POLITECNICO DI TORINO
Repository ISTITUZIONALE

Patient-specific Biomechanical Investigation of Percutaneous Pulmonary Valves: Towards the Integration of Routinely Acquired Clinical Data and Fluid-structure Interaction

Original
Patient-specific Biomechanical Investigation of Percutaneous Pulmonary Valves: Towards the Integration of Routinely Acquired Clinical Data and Fluid-structure Interaction Simulations / Arminio, M., Carbonaro, D., Gallo, D., Paz, R.R., Pin, F.D., Morbiducci, U., Schievano, S., Chiastra, C., Capelli, C.. - In: IEEE JOURNAL OF BIOMEDICAL AND HEALTH INFORMATICS. - ISSN 2168-2194. - ELETTRONICO. - PP:(2026), pp. 1-14. [10.1109/jbhi.2026.3708991]

Availability:
This version is available at: 11583/3018016 since: 2026-11-17T11:54:00Z

Publisher:
Institute of Electrical and Electronics Engineers

Published
DOI:10.1109/jbhi.2026.3708991

Terms of use:

This article is made available under terms and conditions as specified in the corresponding bibliographic description in the repository

Publisher copyright

(Article begins on next page)

21 November 2026

Patient-Specific Biomechanical Investigation of Percutaneous Pulmonary Valves: Toward the Integration of Routinely Acquired Clinical Data and Fluid-Structure Interaction Simulations

Mariachiara Arminio, Dario Carbonaro, Diego Gallo, Rodrigo R. Paz, Facundo Del Pin, Umberto Morbiducci, Silvia Schievano, Claudio Chiastra, and Claudio Capelli

***Abstract*—Percutaneous pulmonary valves (PPVs) offer a minimally invasive option to treat pulmonary valve dysfunction in patients with congenital heart disease. Fluid-structure interaction (FSI) simulations can provide a comprehensive assessment of heart valves biomechanics by capturing the coupled hemodynamics and leaflet mechanics. However, their application to PPVs remains limited. As the range of commercially available devices expands, robust characterization of PPV biomechanics may support the evaluation of short and long-term treatment performance. In this context, this study presents a patient-specific FSI framework for PPV simulation based on routinely acquired clinical data. Pulmonary artery and bifurcation geometries from four patients with implanted PPV were reconstructed from computed tomography. A PPV model was created and positioned within each patient-specific geometry. Boundary conditions were prescribed using patient-specific flow-rate waveforms and flow splits. Two-way, strongly coupled FSI simulations were performed to quantify transvalvular pressure drop, PPV-related flow patterns, and leaflets mechanics. Simulations reproduced peak transvalvular pressure drop in good agreement with available clinical measurements. Hemodynamics varied markedly across patients, with inter-patient differences up to 393% in vorticity stretching and 337% in helicity intensity. Leaflet mechanics provided insights into the distribution of wall shear stress and first principal stress on PPV leaflets. Overall, the FSI approach captured PPV biomechanics across diverse patient-specific scenarios matching clinical pressure measurements and providing additional information on PPV biomechanical behavior. These results support the potential use of patient-specific FSI modelling to investigate PPV behavior under different patient-specific operating conditions.**

***Index Terms*—Fluid-structure interaction, heart valve prosthesis, patient-specific modeling, percutaneous pulmonary valve, pulmonary valve replacement.**

I. Introduction

CONGENITAL heart disease affects approximately 1–2% of live births, and in about 20% of cases involves anomalies of the right ventricular outflow tract (RVOT) and/or the pulmonary valve [1], [2], [3]. For patients requiring treatment of RVOT dysfunction, percutaneous pulmonary valve implantation (PPVI), involving the implantation of a transcatheter valve in the pulmonary position, has become a standard-of-care therapy [4]. Leveraging its minimal invasiveness, PPVI can reduce the cumulative number of open-heart surgeries over a patient's lifetime and is associated with a lower rate of procedure-related complications compared to surgical valve replacement [3], [5]. Since its introduction in the early 2000s, PPVI adoption has grown substantially, with over 11000 procedures reported and a steadily expanding range of PPV designs developed to accommodate heterogeneous anatomies and broaden patient eligibility [4], [6], [7], [8], [9].

Device biomechanics is a key determinant of clinical outcomes after PPVI, as unfavorable mechanical loading may be responsible for post-procedural complications [10]. Prior work has primarily focused on PPV stent-related failure mechanisms, particularly stent fracture, which can precipitate acute valve dysfunction necessitating reintervention [11], [12]. However, as

Received 6 March 2026; revised 29 May 2026; accepted 27 June 2026. This work involved human subjects in its research. Approval of all ethical and experimental procedures and protocols was granted by Institutional Review Board Statement - UCL Review Board under R&D No. 20HL15 and No. REC: 06/Q0608/124. *(Corresponding author: Claudio Chiastra.)*

Mariachiara Arminio, Diego Gallo, Umberto Morbiducci, and Claudio Chiastra are with the PolitoBIOMed Lab, Department of Mechanical and Aerospace Engineering, Politecnico di Torino, 10129 Turin, Italy (e-mail: mariachiara.arminio@polito.it; diego.gallo@polito.it; umberto.morbiducci@polito.it; claudio.chiastra@polito.it).

Dario Carbonaro is with the PolitoBIOMed Lab, Department of Mechanical and Aerospace Engineering, Politecnico di Torino, 10129 Turin, Italy, and also with the Department of Mechanical, Energy and Management Engineering, University of Calabria, 87036 Rende, Italy (e-mail: dario.carbonaro@unical.it).

Rodrigo R. Paz is with Ansys/Synopsys, Inc., Livermore, CA 94085 USA, and also with the CONICET, National Council for Scientific and Technical Research, Buenos Aires C1425FQB, Argentina (e-mail: rodrigo.paz@ansys.com).

Facundo Del Pin is with Ansys/Synopsys, Inc., Livermore, CA 94085 USA (e-mail: facundo.delpin@ansys.com).

Silvia Schievano and Claudio Capelli are with the Institute of Cardiovascular Science, University College London, WC1E 6BT London, U.K., and also with the Great Ormond Street Hospital for Children, WC1N 3JH London, U.K. (e-mail: s.schievano@ucl.ac.uk; c.capelli@ucl.ac.uk).

This article has supplementary downloadable material available at https://doi.org/10.1109/JBHI.2026.3708991, provided by the authors.

Digital Object Identifier 10.1109/JBHI.2026.3708991

© 2026 The Authors. This work is licensed under a Creative Commons Attribution 4.0 License. For more information, see https://creativecommons.org/licenses/by/4.0/

longer-term follow-up data accumulate, attention has increasingly shifted toward long-term performance-limiting phenomena that may depend on local hemodynamics, including valve degeneration and subclinical leaflet thrombosis [13], [14]. These observations motivate a more comprehensive characterization of the coupled fluid and structural mechanics governing PPV performance *in vivo*.

Simulations can support the biomechanical investigation of pulmonary valve substitutes, allowing for the exploration of various device operating conditions. Previous studies have applied structural finite element analysis and computational fluid dynamics to assess, respectively, mechanical stresses and flow patterns associated with PPVs [15], [16], [17], [18], [19], [20]. However, these approaches do not allow for the simultaneous analysis of structural mechanics and fluid dynamics, thereby limiting the overall comprehensiveness of device performance evaluation. Fluid-structure interaction (FSI) modelling addresses this limitation by resolving the coupled interaction between the valve and blood flow. FSI simulations have been widely used to characterize the behavior of aortic and mitral valve prostheses, attempting to link biomechanics to adverse events, support *in silico* evaluation of device designs, and inform device selection and surgical planning [21], [22], [23], [24], [25], [26], [27], [28]. In several studies, FSI simulations based on clinical data evaluated virtually patient-specific performance of an implanted valve, fostering personalized medicine applications such as adverse-event prediction and clinical decision support [25], [29], [30], [31]. However, few FSI studies have targeted pulmonary valve prostheses, with patient-specific FSI simulations of PPVs that remain still largely unexplored.

The aim of this study is to develop a FSI framework for the patient-specific simulation of PPVs using routinely acquired clinical data. The proposed patient-specific FSI framework is evaluated in four patients with implanted PPVs spanning diverse anatomical features and baseline hemodynamics. In addition, to investigate clinically relevant functional impairment, the FSI framework is used to compare device behavior in two of the selected patients before and after valve narrowing.

II. Methods

A. Patient Population

Four patients who underwent implantation of the Melody PPV (Medtronic, Dublin, IR) at Great Ormond Street Hospital for Children (London, UK) between 2014 and 2017 were retrospectively selected. The inclusion criteria were: (i) computed tomography (CT) imaging of the pulmonary arteries (PAs) acquired after PPVI; (ii) right/left PA flow split quantified by magnetic resonance imaging (MRI), and (iii) Doppler echocardiography conducted both prior to discharge after PPVI and the time of CT imaging. Institutional ethical approval for the retrospective use of patients' data was obtained (Institutional Review Board Statement - UCL review board under R&D number 20HL15 and REC: 06/Q0608/124).

The four selected patients encompassed heterogeneous underlying congenital diagnoses and prior surgical histories. These included the implantation and multiple replacements of a right ventricle-to-PA conduit for patient A, Blalock-Taussig shunts and Rastelli operation for patient B, Ross procedure and conduit implantation for patient C, and Tetralogy of Fallot repair with subsequent conduit implantation for patient D. CT imaging showed severe narrowing and flattening of the proximal PPV in patient A due to stent fracture, and mild PPV narrowing in patient C. MRI was acquired three years after CT in patient A, within one year of CT in patients B and D, and six years after CT in patient C. Demographic characteristics and pulmonary flow-split measurements are reported in Table I.

B. Simulation Scenarios

For each of the four patients, a follow-up scenario was simulated corresponding to the time point of CT scan acquisition (Table I). Additionally, for patients A and C, a post-PPVI scenario corresponding to the immediate post-implantation phase, characterized by the absence of valve narrowing, was simulated. The follow-up scenarios for the four patients are hereafter referred to as A_{FU}, B_{FU}, C_{FU}, and D_{FU}, whereas the post-PPVI scenarios for patients A and C are hereafter referred to as A_{PPVI} and C_{PPVI}.

C. Geometrical Model

1) Pulmonary Arteries and Bifurcation Model: For each patient, a three-dimensional model of the PAs and bifurcation was reconstructed from CT images by segmentation in Simpleware (Synopsys, Sunnyvale, CA, USA) (Fig. 1). Segmentation was initiated using a threshold-based greyscale approach (Hounsfield units 220-600) and subsequently refined by manual correction of luminal contours on each slice. The reconstructed domain extended from the main pulmonary artery (MPA) through the right (RPA) and left (LPA) pulmonary arteries up to the first daughter branch of each vessel (Fig. 2). To reduce boundary-condition sensitivity and numerical artefacts, straight flow extensions were appended to the RPA and LPA outlets with a length equal to three equivalent diameters. In patients A and C, an additional post-PPVI geometry representing a configuration without PPV narrowing was reconstructed starting from the segmented follow-up configuration. To do this, for both patients procedural reports and fluoroscopy measurements were used to retrieve the expansion diameter of the balloon used for valve deployment. Based on this information, the post-PPVI PA geometrical models were obtained by manually modifying the follow-up models so that the MPA diameter matched the PPVI balloon diameter (Fig. 2).

2) Valve Model: A geometrical model of the Melody PPV was generated in SolidWorks (Dassault Systèmes, Vélizy-Villacoublay, FR), based on measurements obtained from valve samples (Fig. 1). The PPV model included three identical leaflets. Leaflet thickness was set to 0.2 mm, with a locally increased thickness of 0.5 mm along the attachment edge. The PPV stent was included in the geometrical model and used to define valve implantation height based on its CT-derived position, although it was not modeled in the FSI simulations.

TABLE I
DEMOGRAPHIC CHARACTERISTICS AND PULMONARY ARTERY FLOW SPLIT FOR THE PATIENTS INCLUDED IN THE STUDY

Patient	Sex	Age at PPVI	Congenital heart disease	Flow split (Q_{RPA}:Q_{LPA})	Months between PPVI and follow-up CT
A	Male	15	Truncus arteriosus	27:72	21
B	Male	10	Pulmonary atresia and transposition of the great arteries	46:54	53
C	Male	13	Aortic stenosis, treated with Ross procedure	54:45	25
D	Female	18	Tetralogy of Fallot	61:39	7

CT: computed tomography; LPA: left pulmonary artery; PPVI: percutaneous pulmonary valve implantation; RPA: right pulmonary artery.

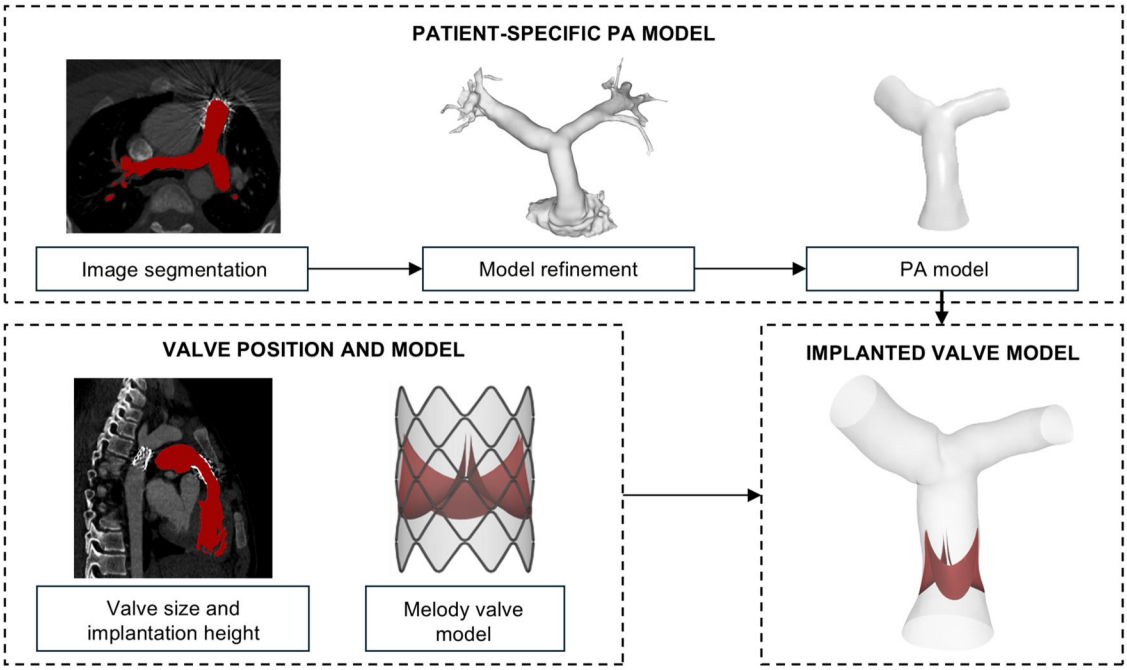


Fig. 1. Generation of the pulmonary artery (PA) and implanted valve model derived from clinical data.

TABLE II
PERCUTANEOUS PULMONARY VALVE SIZE, INLET BLOOD VELOCITY WAVEFORM CHARACTERISTICS DERIVED FROM DOPPLER ECHOCARDIOGRAPHY, AND OUTLET RESISTANCE BOUNDARY CONDITIONS FOR THE FLUID-STRUCTURE INTERACTION SCENARIOS

Simulation scenario	PPV size (mm)	Heart rate (bpm)	Systole (s)	Flow acceleration (s)	Maximum blood velocity (m/s)	R_{RPA} (MPa·s/m^3)	R_{LPA} (MPa·s/m^3)
A_{PPVI}	15	77	0.33	0.12	3.8	118.7	15.4
A_{FU}	12	75	0.41	0.19	5.4	105.0	17.5
B_{FU}	16	59	0.45	0.17	3.1	25.2	37.0
C_{PPVI}	18	83	0.33	0.12	2.9	24.0	40.0
C_{FU}	15	94	0.36	0.18	3.2	24.0	40.0
D_{FU}	14	63	0.42	0.19	3.1	30.0	30.0

D. Simulation Domain and Discretization

The computational domain comprised the PAs and bifurcation, with embedded PPV leaflets. Valve leaflets were incorporated into the fluid domain through a morphing process using HyperMesh (Altair Engineering Inc., Troy, MI, USA). Specifically, the valve was first positioned in proximity to the MPA and then scaled to achieve correspondence between valve and arterial diameter along most of the valve length (Table II). Then, the idealized leaflet geometry (Fig. 1) was automatically

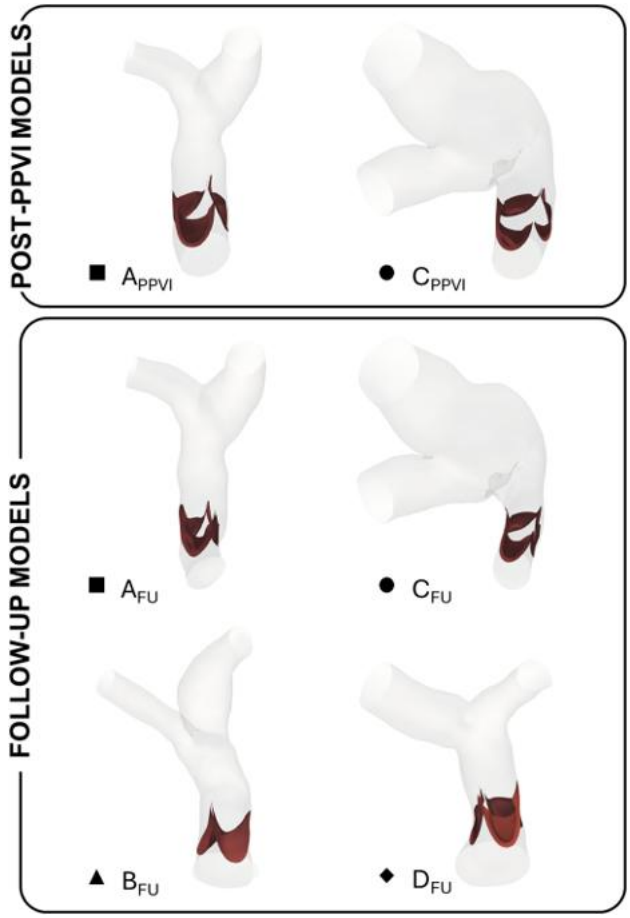


Fig. 2. Geometrical models for the six simulated scenarios. FU: Follow-up; PPVI: Percutaneous pulmonary valve implantation.

adapted to conform to the patient-specific lumen shape while preserving leaflet surface area, thereby accounting for the geometrical variation in leaflet shape induced by PPVI (Fig. 2). PPV implantation height was selected to match the PPV stent position observed on CT images. Leaflets commissural orientation was assumed to be analogous to that of the native pulmonary valve with one leaflet opening posterior [32]. PAs were modeled as rigid structures, i.e., vessel wall deformation was neglected.

Meshing was performed in HyperMesh. The surface of the computational domain was discretized with triangular shell elements. Spatial resolution was locally refined in regions of interest: the vessel wall surface was discretized with a characteristic element size of 0.4 mm in the leaflet region and 1.0 mm elsewhere. PPV leaflets were discretized using first-order shell elements with a characteristic element size of 0.1 mm along the free edge and 0.3 mm in the remaining leaflet area. These mesh resolutions are consistent with prior computational studies where authors performed a mesh sensitivity study [33], [34]. A volumetric fluid mesh was generated automatically by the ICFD solver from the surface mesh. To enable the interaction between fluid and PPV leaflets, fluid counterparts of the leaflets were embedded within the fluid domain. These embedded "fluid leaflets" shared the same geometry and surface mesh as the structural leaflets.

E. Material Properties

PPV leaflets were modelled as a nearly incompressible, linear elastic material with density equal to 1100 kg/m^3, elastic modulus equal to 0.3 MPa, and Poisson's coefficient equal to 0.495 [35]. Blood was modelled as a homogeneous, incompressible, Newtonian fluid, with density equal to 1060 kg/m^3 and dynamic viscosity equal to 3.7 cP.

F. Boundary Conditions

At the inlet of the MPA, a patient-specific velocity waveform was prescribed using a spatially uniform (plug) profile. To limit uncertainties associated with Doppler-derived flow-rate waveform reconstruction, the waveform shape was derived from the representative pulmonary flow-rate waveform defined in ISO Standard 5840:2021 [36] and stretched to match echocardiographic measurements of heart rate and the durations of systole, diastole, and the flow acceleration and deceleration phases (Fig. 3, Table II). The velocity waveform amplitude was then scaled such that the peak MPA velocity matched the peak Doppler measurement. At the RPA and LPA outlets, boundary conditions were implemented as pure resistances (Fig. 3) [37]. Baseline outlet resistances were assumed to yield an equivalent total resistance of 15 MPa·s·m^{-3} [37]. Individual resistance values at RPA and LPA outlets were tuned to match the patient-specific flow split measured through MRI within a 3% tolerance. Pure resistance boundary conditions were adopted consistently with the unavailability of patient-specific LPA and RPA pressure data needed to estimate downstream vascular compliance. The final resistance values used for each simulation scenario are reported in Table II. The no-slip condition was applied at the fluid-structure interface. For patients A and C, post-PPVI and follow-up echocardiographic data were available, enabling the definition of distinct inlet flow-rate waveforms for post-PPVI and follow-up scenarios. Matching the patient-specific flow split required different outlet resistance values at follow-up compared with post-PPVI in patient A, but not in patient C.

G. Solver Set-Up

The two-way interaction between the blood flow and PPV leaflets was simulated using the finite-element incompressible fluid solver of LS-DYNA (ICFD), which is strongly coupled with its implicit structural solver (Ansys Inc., Canonsburg, PA, USA) to mitigate numerical instabilities and ensure convergence of the results at the fluid–structure interface [33]. The fluid domain was solved using a boundary-fitted arbitrary Lagrangian-Eulerian formulation to accommodate the large mesh deformations associated with leaflet dynamics [33]. Convergence tolerances were set to 10^{-12} for both momentum and pressure equations, with a maximum number of iterations allowed to achieve convergence equal to 2000. Based on a previous study where authors performed a results repeatability analysis [34], for each scenario two cardiac cycles were simulated, and results were extracted from the second one. Based on the peak and mean systolic Reynolds numbers at the MPA inflow section (mean Reynolds number across scenarios: 3711 - 7024; peak systolic Reynolds number

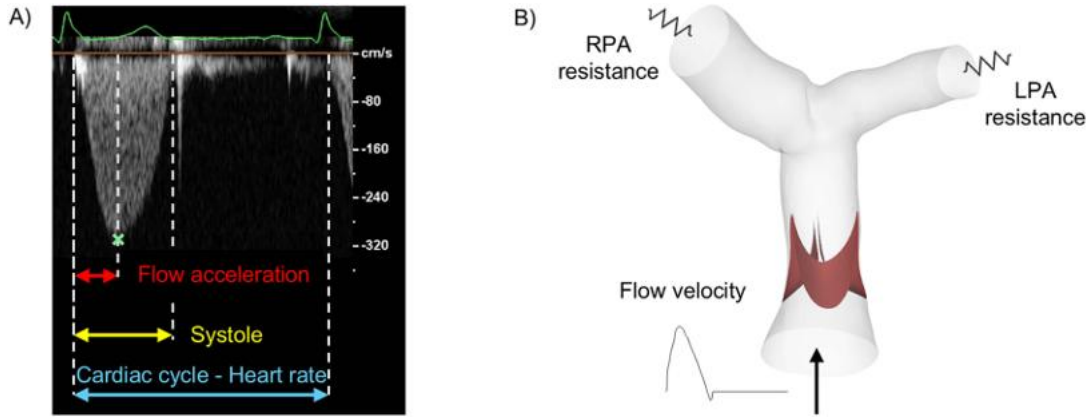


Fig. 3. Boundary conditions for fluid-structure interaction simulations. (a) Flow velocity information retrieved from Doppler echocardiography. (b) Boundary conditions applied at the inflow and outflow sections of a representative model. LPA: Left pulmonary artery; RPA: Right pulmonary artery.

across scenarios: 6121 - 11408) turbulence modelling was included via a standard k-ϵ model with a standard classic law of the wall, consistent with prior studies [38], [39], [40]. The structural problem was solved using a fully implicit finite-element formulation with time integration handled by the LS-DYNA implicit solver [41]. Leaflet coaptation was modelled by activating an automatic single-surface Mortar contact, a penalty-based contact defined in LS-DYNA [30]. The ICFD and initial Lagrangian time steps were set to 0.5 ms and 1 ms, respectively, thereby ensuring that the FSI time step was dictated by the fluid solver. The average computational time required to solve each cardiac cycle was approximately 14.5 hours on 64 cores of a workstation equipped with Intel Xeon Gold 6338 CPU@2.00GHz and 64 GB RAM.

H. Results Analysis

Peak systolic transvalvular pressure drop from FSI simulations was compared with clinical measurements from post-PPVI catheterization and Doppler echocardiography. For patient D, a follow-up Doppler-derived pressure drop was not available. Therefore, the simulated follow-up pressure drop was compared with the post-PPVI catheterization value, noting that a higher gradient is expected at follow-up in light of PPV narrowing.

Hemodynamics was evaluated in terms of velocity fields, vorticity transport, helical flow, viscous dissipation rate, and wall shear stress (WSS). Coherent vortical structures were visualized using the Q-criterion, which identifies regions where local fluid rotation dominates over fluid strain [42]. Vorticity was additionally quantified in terms of vorticity stretching, which measures the rate at which vorticity is amplified because of the deformation of vortex tubes in the flow field [43], [44]. The stretching was averaged both over the volume of the simulation domain except for the flow extensions and over the cardiac cycle. Helical flow was quantified through local normalized helicity (LNH, which measures the local alignment between velocity and vorticity vectors) and helicity-based descriptors h_2 and h_4, describing, respectively, the cycle-average, volume-average helical flow intensity and the balance between counter-rotating helical fluid structures in the flow field [45]. To provide an indicator of blood flow energy losses, viscous dissipation rate was computed, divided by the simulation domain volume except for the flow extensions, and averaged over the cardiac cycle [46].

The hemodynamic load exerted on the luminal surface of PAs was characterized using the time-averaged wall shear stress (TAWSS) to quantify the average WSS magnitude over the cardiac cycle, and the oscillatory shear index (OSI) to quantify WSS directional changes over the cardiac cycle.

Leaflets biomechanics was analyzed using leaflet TAWSS and first principal stress. Leaflet kinematics was quantified via projected orifice area, defined as the area of the largest open region enclosed by PPV leaflets when projected onto a reference plane [47], [48].

III. Results

A. Transvalvular Pressure Drop

Transvalvular pressure-drop waveforms for all simulated scenarios are reported in Fig. 4. Peak transvalvular pressure drops predicted by FSI simulations agreed well with the corresponding clinical measurements (Table III). Comparison between early post-PPVI and follow-up (i.e., A_{PPVI} vs. A_{FU}, and C_{PPVI} vs. C_{FU}) indicated higher pressure gradients in the follow-up scenarios, consistent with PPV narrowing observed on CT. Peak pressure drop increased by factors of 1.8 (patient A) and 2.4 (patient C).

B. Common Flow Features Across Simulation Scenarios

Several flow features arising from the interaction between PPV leaflets and PA hemodynamics were consistently observed across all cases. The temporal evolution of pulmonary hemodynamics in terms of velocity streamlines, Q-criterion isosurfaces, and helical structures is illustrated in Fig. 5 and in the Supplementary Video for D_{FU} as a representative example. During early systolic acceleration, progressive leaflet opening

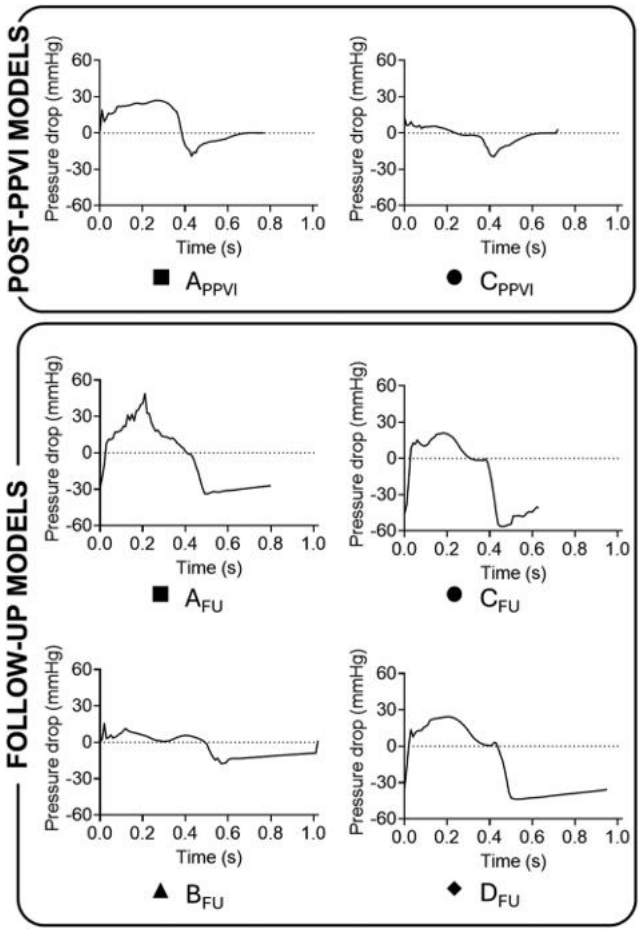


Fig. 4. Transvalvular pressure drop waveforms for fluid-structure interaction simulations.

TABLE III
PEAK TRANSVALVULAR PRESSURE DROP: CLINICAL MEASUREMENTS VERSUS FLUID-STRUCTURE INTERACTION SIMULATIONS

Simulation scenario	Peak pressure drop from clinical measurement (mmHg)	Peak pressure drop from FSI simulation (mmHg)	Percentage difference (%)
A_{PPVI}	26	27	+3.8
A_{FU}	52	49	-5.8
B_{FU}	12	15	+25.0
C_{PPVI}	10	9	-10.0
C_{FU}	NA	22	NA
D_{FU}	18	24	+33.3

NA: not accessible.

increased flow complexity throughout the PAs (Fig. 5(a)–(b)). A three-lobed vortex structure was shed by the leaflets and convected distally, while additional vortex structures formed in the MPA proximal to the bifurcation. With increasing flow rate, helical flow became evident within both the RPA and LPA, with helical fluid structures increasing in spatial extent

TABLE IV
TIME- AND VOLUME-AVERAGED STRETCHING MAGNITUDE AND VISCOUS DISSIPATION RATE, AND HELICAL FLOW DESCRIPTORS (H_2, H_4) FOR THE FLUID-STRUCTURE INTERACTION SIMULATIONS

Simulation scenario	Stretching magnitude (s^{-2})	Viscous dissipation rate (W/m^3)	h_2 (m/s^2)	h_4
A_{PPVI}	15728	905	54.6	0.30
A_{FU}	16509	896	33.2	0.05
B_{FU}	10203	717	22.6	0.06
C_{PPVI}	3349	157	12.7	0.18
C_{FU}	4302	230	12.5	0.04
D_{FU}	16003	945	34.2	0.05

and intensity over systole. At peak systole, velocity streamline visualization revealed highly complex flow patterns, particularly in the bifurcation region, where multiple vortex structures were present (Fig. 5(c)). These patterns persisted into late systole and early deceleration phases, with a progressive reduction in velocity magnitudes (Fig. 5(d)). At the time of peak reverse flow, when the PPV leaflets were closed, velocities were low and vortical activity was markedly reduced (Fig. 5(e)).

C. Patient-Specific Biomechanics in Follow-Up Scenarios

Inter-patient hemodynamic variability is shown in Figs. 6–7. Instantaneous velocity streamline visualizations at peak systole highlighted that hemodynamics differed across A_{FU}-D_{FU} both near the bifurcation region and within the branch PAs (Fig. 6). In A_{FU} and C_{FU}, the blood jets entering the RPA and LPA exhibited comparable velocity magnitudes, whereas in B_{FU} and D_{FU} higher velocities were observed in the RPA than in the LPA. At peak systole, widespread vortex structures were present in all follow-up scenarios (Fig. 7(a)). Specifically, in A_{FU} and D_{FU}, large-scale vortices originated in the PPV region and extended downstream toward the bifurcation, possibly driven by MPA curvature. In B_{FU} and D_{FU}, additional vortex structures were also visible near leaflet tips. Helical flow organization also varied across patients (Fig. 7(b)). Counter-rotating helical fluid structures were clearly visible distal to the PPV leaflets in A_{FU}, B_{FU}, and D_{FU}. In D_{FU}, the two counter-rotating helical structures propagated into the branch arteries. Conversely, in A_{FU}, helical flow structures of the same rotational sense established in both the LPA and RPA, while in B_{FU} a single helical structure was observed in the LPA.

Over the full cardiac cycle, quantitative intravascular flow metrics (Table IV) showed that C_{FU} exhibited the lowest mean vorticity stretching magnitude and the lowest value of h_2. Additionally, all follow-up scenarios exhibited h_4 values lower than 0.06, indicating an overall balance between counter-rotating helical fluid structures across the cardiac cycle. Viscous dissipation rate was lowest in C_{FU} and highest in D_{FU}, with an approximately fourfold difference between these scenarios (Table IV).

The analysis of WSS-based descriptors at the arterial wall is shown in Fig. 8. In all follow-up models, interaction between

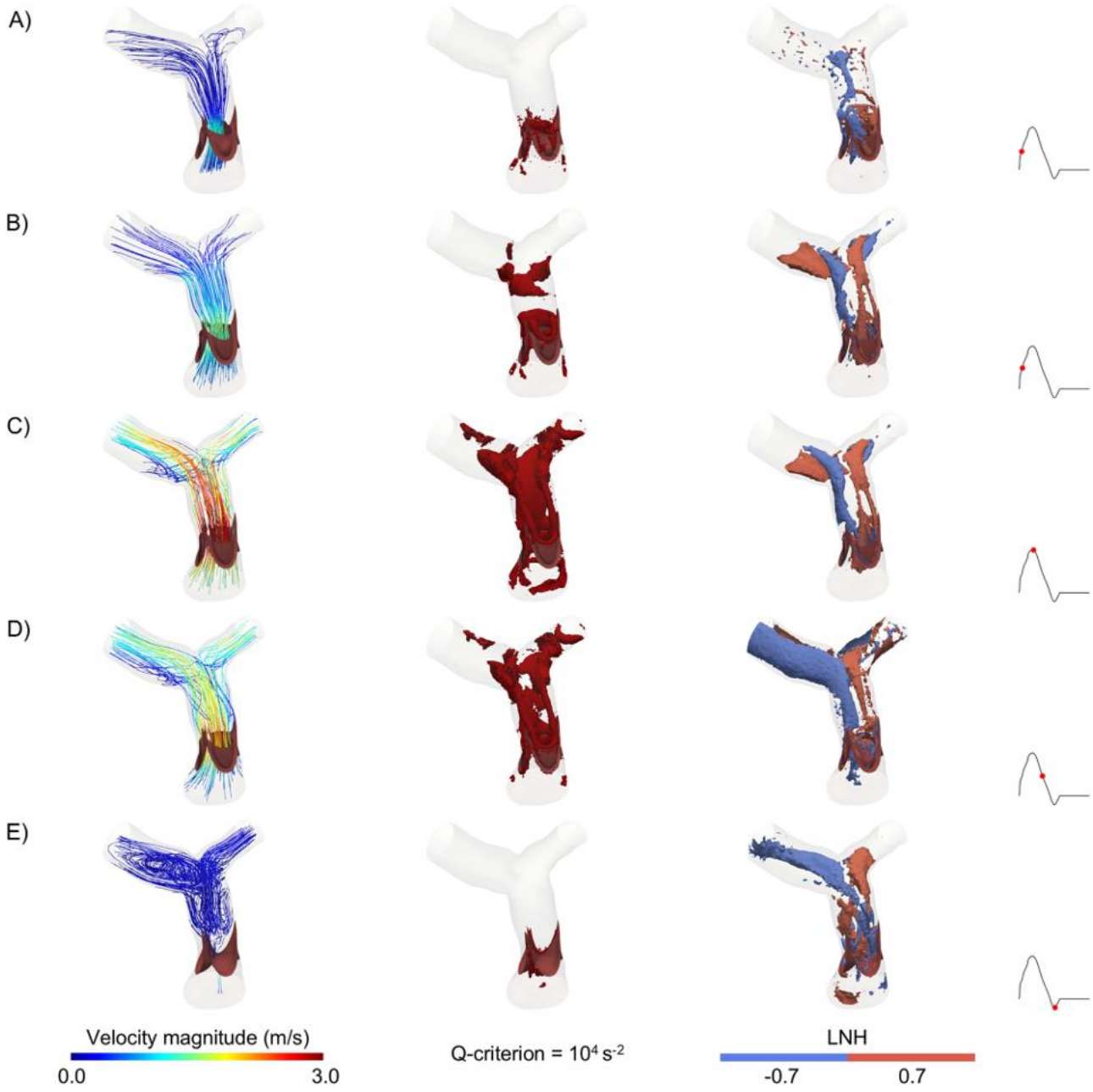


Fig. 5. Intravascular hemodynamics for simulation scenario D_{FU} over the cardiac cycle: (a)-(b) during flow acceleration; (c) at peak systole; (d) during flow deceleration; and (e) at the negative flow-rate peak. Hemodynamics is shown in terms of velocity streamlines colored by velocity magnitude (left), Q-criterion isosurfaces ($Q = 10^4$ s^{-2}) (center), and LNH isosurfaces highlighting helical right-handed (LNH $= 0.7$, red) and left-handed (LNH $= -0.7$, blue) fluid structures (right).

the transvalvular jet and the local curvature in the PPV region resulted in elevated TAWSS on the anterior wall proximal to the bifurcation, whereas low-TAWSS regions were observed in the proximal segments of both RPA and LPA (Fig. 8(a)). OSI was generally low across the domain, with localized increases in the proximal branch arteries and near the leaflet attachment edge (Fig. 8(b)).

On the leaflet surface, the highest TAWSS were observed along the free edge (Fig. 9). Peak-systolic first principal stress maps showed comparable stress distributions across all follow-up scenarios, with peak values of approximately 0.05 MPa (Fig. 10). Leaflet kinematics indicated that the PPV reached the maximum values of projected orifice area by mid-acceleration phase and initiated closure at flow rate reversal in all follow-up scenarios (Fig. 11). In A_{FU}, the projected orifice area showed small-amplitude oscillations during systole, consistent with flutter-like behavior.

D. Effect of Valve Narrowing

Differences between post-PPVI and follow-up scenarios for patients A and C are shown at peak systole in Figs. 6–7. In patient

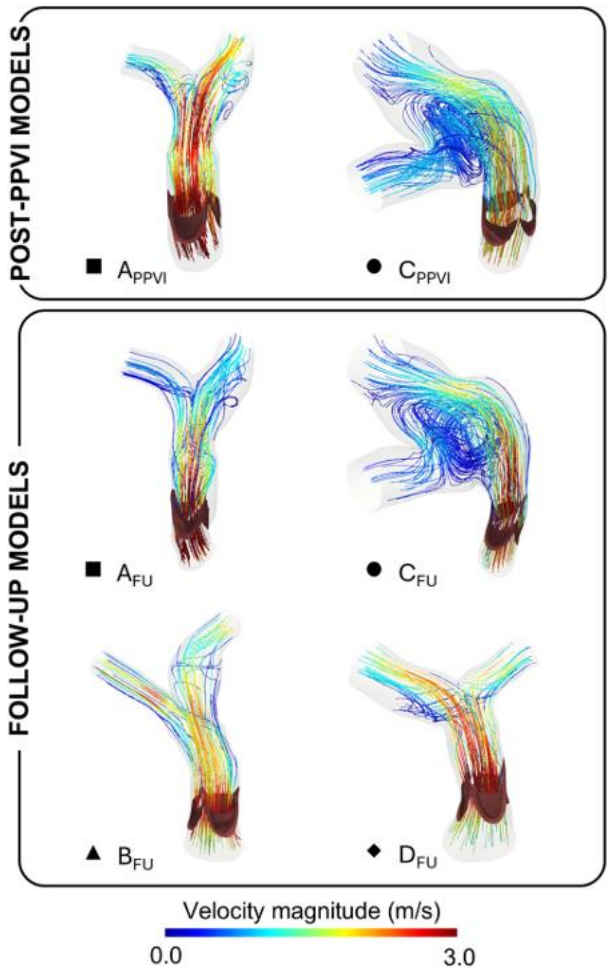


Fig. 6. Velocity streamlines at peak systole for the six simulation scenarios.

C, PPV narrowing increased peak velocities in the leaflet region, whereas the overall flow organization remained qualitatively similar between C_{PPVI} and C_{FU} (Fig. 6). For both patients A and C, peak-systolic vortex and helical fluid structures occupied larger regions in the post-PPVI than in the corresponding follow-up (Fig. 7).

Across the full cardiac cycle, the intravascular flow quantities (Table IV) indicated changes in flow organization and energy losses, associated with PPV narrowing. Time-averaged vorticity stretching magnitude was higher in A_{FU} and C_{FU} than in A_{PPVI} and C_{PPVI}. For patient A, h_2 decreased by 39% in A_{FU} relative to A_{PPVI}, indicating reduced overall helical flow intensity at follow-up, whereas h_2 remained nearly unchanged between C_{PPVI} and C_{FU}. In both patients, h_4 was lower at follow-up than post-PPVI, consistent with a shift toward a more balanced contribution of counter-rotating helical components. Viscous dissipation rate increased by 46% from C_{PPVI} to C_{FU}, indicating higher flow energy losses in the follow-up configuration for patient C (Table IV). In contrast, viscous dissipation was very similar between A_{PPVI} and A_{FU} (difference $< 1\%$, Table IV).

TAWSS patterns at the arterial wall also differed between post-PPVI and follow-up models, with higher values observed in the RPA and LPA in the post-PPVI scenarios (Fig. 8(a)). OSI showed a modest increase in the proximal branch arteries in the follow-up configurations for both patients (Fig. 8(b)).

At the leaflet surface, follow-up scenarios exhibited higher TAWSS and first principal stress than the corresponding post-PPVI configurations (Figs. 9–10). Peak first principal stress increased by approximately a factor of two at follow-up in both patients (Fig. 10). Leaflet kinematics reflected functional impairment: projected orifice area was markedly reduced during systole in A_{FU} and C_{FU} compared with A_{PPVI} and C_{PPVI}, respectively (Fig. 11).

IV. Discussion

Pulmonary valve prostheses have been scarcely investigated through the FSI approach, and the capability of the available studies [37], [49], [50] to accurately capture their biomechanics is limited by the use of reduced–degree-of-freedom leaflet models [37], [49] and by modelling devices not specifically intended for the pulmonary position [37], [50]. In this context, the present study represents the first attempt to conduct FSI simulations of a commercially available PPV in a patient-specific setting while accounting for all degrees of freedom of valve leaflets. In this study, a patient-specific FSI framework that integrates numerical simulations with routinely acquired clinical data was developed to characterize the biomechanics of PPVs. The framework was applied to four patients spanning heterogeneous congenital anatomies and hemodynamic conditions, including two cases in which follow-up imaging indicated PPV narrowing (A_{FU}, C_{FU}). Although the limited number of investigated scenarios precludes general conclusions of clinical relevance, this study highlights how FSI modelling can provide mechanistic insights into the biomechanics of implanted PPVs as shaped by the interaction among PPV leaflets, anatomy, and blood flow [26], [51], [52].

The proposed FSI simulations reproduced peak transvalvular pressure drop with good agreement against available clinical estimates, with the largest overestimation and underestimation observed in D_{FU} and C_{PPVI}, respectively. Although this quantity represents a single time-point descriptor of PPV performance, peak transvalvular pressure drop is clinically relevant for grading pulmonary outflow [53]. Specifically, in the setting of RVOT obstruction, peak gradients below 36 mmHg are classified as mild, values between 36 and 64 mmHg as moderate, and values above 64 mmHg as severe [54]. Across the six simulated scenarios, FSI predictions assigned each case to the same RVOT obstruction severity category as the corresponding clinical estimate (mild in all cases except B_{FU}, which was classified as moderate). This agreement was obtained across heterogeneous anatomies shaped by patient-specific morphology and prior surgical interventions, including scenarios with markedly imbalanced pulmonary flow split (A_{PPVI} and A_{FU}). PPV narrowing determined an increased pressure drop in A_{FU} and C_{FU} relative to the corresponding post-PPVI configurations.

Across all cases, the analysis revealed the formation of a three-lobed tip vortex ring during systolic acceleration phase, the subsequent breaking down of the tip vortex ring into smaller

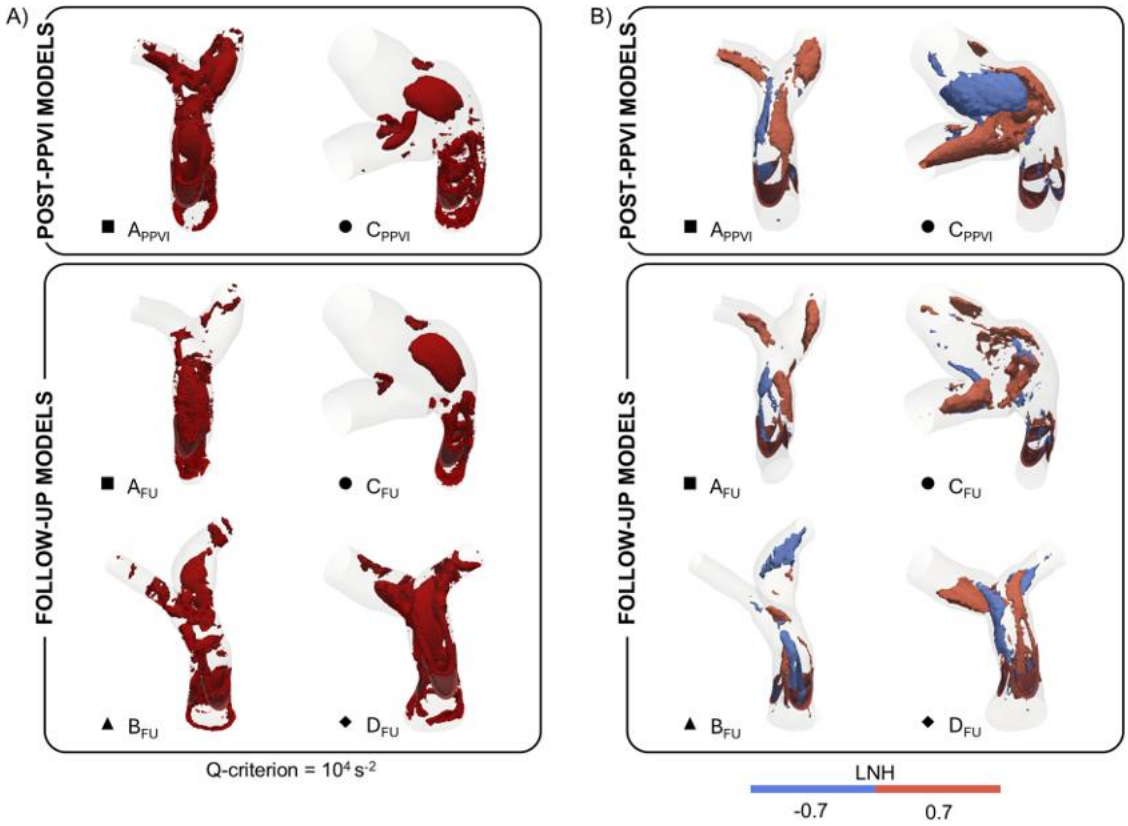


Fig. 7. Intravascular flow structures at peak systole for the six simulation scenarios: (a) Q-criterion isosurfaces illustrating vortical regions ($Q = 10^4$ s^{-2}); (b) local normalized helicity (LNH) isosurfaces highlighting helical right-handed (LNH = 0.7, red) and left-handed (LNH = −0.7, blue) fluid structures.

scale vortex structures during late acceleration, the progressive attenuation of the forward jet during deceleration, and the comparatively quiescent diastolic hemodynamics. All these phenomena have been extensively documented downstream of biological valve prostheses [37], [55], [56].

Individual anatomy modulated the prominence of distinct flow patterns. At peak systole, low-velocity regions characterized blood flow along the inner wall of the MPA [50], [57] and were most pronounced in patients B and C. Branch-vessel curvature in the RPA and LPA produced a characteristic redistribution of momentum, with reduced velocity along the intrados and displacement of the high-speed jet toward the outer wall [58], [59]. Consistent with this shift, a flow separation region formed distally and was generally more evident in the LPA than in the RPA, except in D_{FU}, supporting previous observations that larger separation zones tend to occur in vessels with larger cross-sectional vessel areas [58]. Additionally, the analysis highlighted that in B_{FU} a portion of flow originating on the left side of the MPA feeds the RPA, in agreement with *in vivo* observations of cross-stream mixing at the bifurcation [60].

Vortex structures formed predominantly within the MPA across all scenarios. In B_{FU} and D_{FU}, additional vortices were observed downstream of the LPA and RPA branching points, consistent with the known influence of bifurcation anatomy on local flow separation and recirculation, particularly in the LPA [61]. In patients A, B, and D, coherent counter-rotating helical flow patterns developed in the MPA, in agreement with previous observations based on MRI [60], [62]. In contrast, patient C did not exhibit appreciable MPA helicity, which may be partly related to reduced MPA curvature, a factor previously associated with attenuated helical motion [62].

Consistent with prior reports, branch PAs tended to exhibit helical flow with a predominant rotational direction. Specifically, right-handed helical flow predominated in the RPA (A_{PPVI}, A_{FU}, C_{PPVI}, C_{FU}, D_{FU}), while left-handed helical flow predominated in the LPA (B_{FU}, C_{PPVI}, D_{FU}) [58], [60]. In this context, FSI simulations can complement *in vivo* identification of unsteady intravascular pulmonary hemodynamics that may be relevant to vascular pathophysiology, including pulmonary hypertension, PA dilation, and wall remodeling [58], [61], [63].

Quantitative analysis of vorticity stretching and viscous dissipation rate indicated that cases with elevated stretching of vorticity also exhibited higher viscous dissipation, consistent with a reduced hemodynamic efficiency. Together, these results support an association between enhanced vorticity transport in PAs and impaired hemodynamic performance.

Analysis of WSS along the PA luminal surface further showed that patient-specific anatomy modulated the location of systolic jet impingement, which coincided with luminal surface areas subject to elevated TAWSS [49]. Localized increases in OSI were observed near flow separation regions in the proximal RPA and LPA, particularly in A_{FU}, C_{PPVI}, C_{FU}, and D_{FU}.

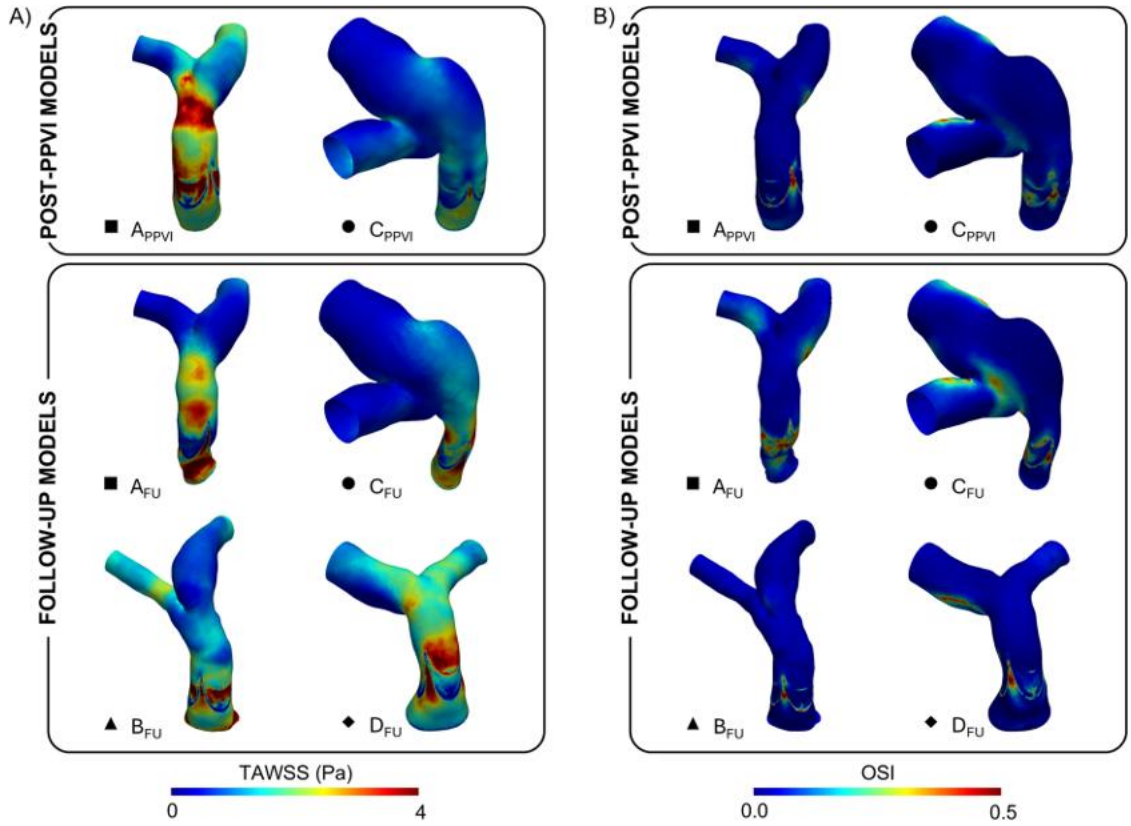


Fig. 8. (a) Time-averaged wall shear stress (TAWSS) and (b) oscillatory shear index (OSI) at the luminal wall for the six simulation scenarios.

Prior studies have suggested that oscillatory shear regions may be subject to increased risk of intimal thickening [64], [65]. Elevated OSI near leaflet commissures was likely ascribable to diastolic backflow and flow reversal during leaflet closure.

Leaflet-surface analysis showed that elevated TAWSS localized nearby the leaflet free edge, whereas first principal stress maps peak values were found mainly in the leaflet belly. The unavailability of investigations reporting stress values for simulated Melody PPV leaflets limits the comparative assessment of the results reported in this study, while also highlighting the potential role of FSI modeling in investigating PPV leaflet biomechanics under physiological conditions. From a kinematic standpoint, systolic projected orifice area varied across scenarios, reflecting patient-specific anatomical and hemodynamic differences. Additionally, the simulations captured leaflet folding, an established feature of highly deformable PPV leaflets consistent with previous reports [66] and visible in C_{PPVI} (Fig. 10).

Finally, the proposed FSI framework leverages clinical data that are routinely acquired in our center for patients undergoing PPVI, including CT, MRI, Doppler echocardiography, and catheterization. These data informed reconstruction of patient-specific anatomy, specification of flow boundary conditions, and consistency-check of model predictions against transvalvular pressure drop measurements. In prior computational studies of PPV biomechanics, patient-specific clinical information has primarily been incorporated into structural finite element models [19], [67], [68], [69], [70]. By integrating routinely available clinical measurements within FSI simulations, this study expands the scope of PPV computational modeling highlighting the role of the FSI approach in characterizing device biomechanical impact and generating hypotheses on PPV functional behavior. Ultimately, further development of patient-specific FSI frameworks may extend these capabilities by providing biomechanical descriptors directly relevant to clinical planning and device evaluation, including assessment of patient suitability, exploration of device design and positioning strategies, and investigation of factors associated with long-term device performance [28], [71]. Since PPVI is typically an elective procedure, the computational costs associated with FSI simulations may not represent a major barrier to their clinical applicability, particularly considering their added value over purely structural simulations for comprehensive PPV assessment in patients with complex anatomies and for the investigation of flow-related phenomena.

This study has several limitations. First, no dedicated experimental validation was performed. Model credibility was evaluated only by comparing simulated peak transvalvular pressure drop with available clinical measurements, owing to the lack of *in vivo* and *in vitro* data on velocity fields and leaflet mechanics. Therefore, future studies should further substantiate model reliability through comparisons with the *in vivo* velocity fields acquired along the cardiac cycle, for example using multi-plane Doppler echocardiography, as well as through dedicated *in vitro* experimental testing. Second, turbulence was modeled using

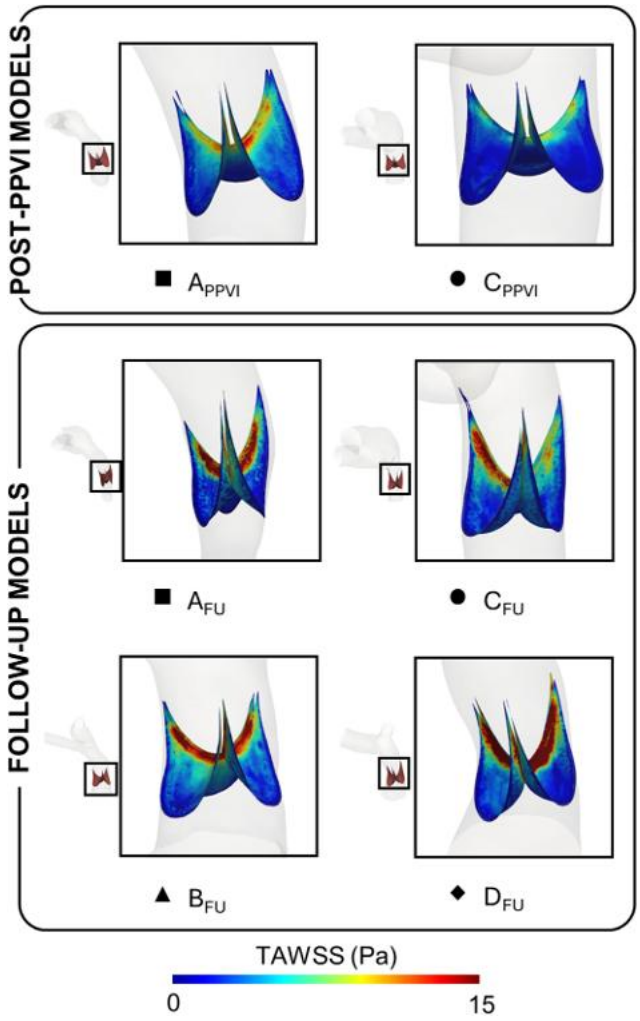


Fig. 9. Time-averaged wall shear stress (TAWSS) at the leaflet surface for the six simulation scenarios.

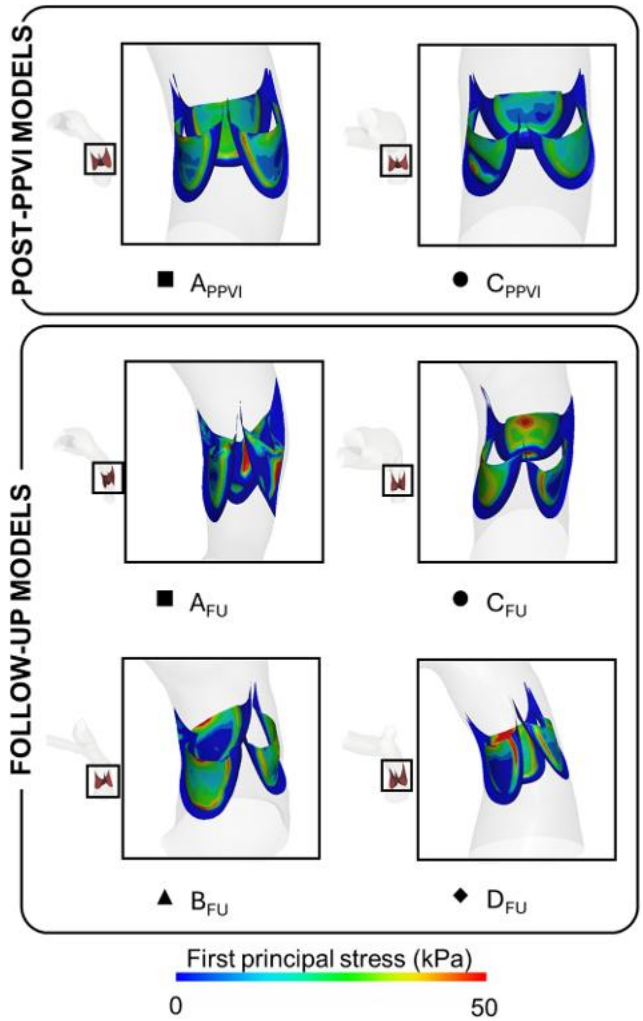


Fig. 10. Peak-systolic distribution of first principal stress in the valve leaflets for the six simulation scenarios.

a RANS approach with a k-ϵ closure. Although higher-fidelity approaches such as large-eddy simulation (LES) may provide a more accurate characterization of transitional and turbulent flow structures relevant to PPV hemodynamics, they also entail substantially greater computational cost and convergence challenges. Therefore, the k-ϵ model was preferred because of its higher numerical robustness, its ability to capture integral hemodynamic quantities such as transvalvular pressure drop, and the fact that detailed characterization of smaller scale fluid structures was outside the scope of the study. Third, the use of a plug-flow velocity profile at the inlet may not fully capture physiological inlet flow conditions. Fourth, the arterial wall was assumed rigid. Accounting for wall deformability would be essential for reliable personalized predictive modelling, particularly in native or patched RVOTs, which undergo large deformations and displacements during the cardiac cycle. However, modeling wall distensibility would substantially increase computational complexity and require reliable estimation of patient-specific wall material properties, which remains challenging because of the marked variability in RVOT mechanical behavior and the limited availability of *in vivo* data suitable for parameter estimation. In the present cohort, all patients had previously undergone RVOT replacement with biological conduits, which are generally stiffer than native or patched RVOTs, thereby reducing the expected impact of the rigid-wall assumption. Fifth, the simulations resolved fluid-leaflet interaction only and the PPV stent was not modelled, although it was used to ensure the positioning of the PPV at the correct implantation height. Stent modelling would allow evaluation of contact forces exerted on the arterial wall, but would require a dedicated implantation simulation, thereby markedly increasing model complexity and computational cost. Nevertheless, the reconstructed fluid domain still allows investigation of the resulting patient-specific hemodynamics. Finally, a linear elastic isotropic material model was adopted for PPV leaflets based on both computational and biomechanical considerations. From a numerical standpoint, this choice limits computational complexity and improves numerical stability. At the same time, experimental evidence supports approximately linear elastic behavior of bovine jugular vein valve leaflets (from which the Melody PPV is derived) up to 25% strain [72], and the strain levels observed in the present simulations remained below this range in particular during systole.

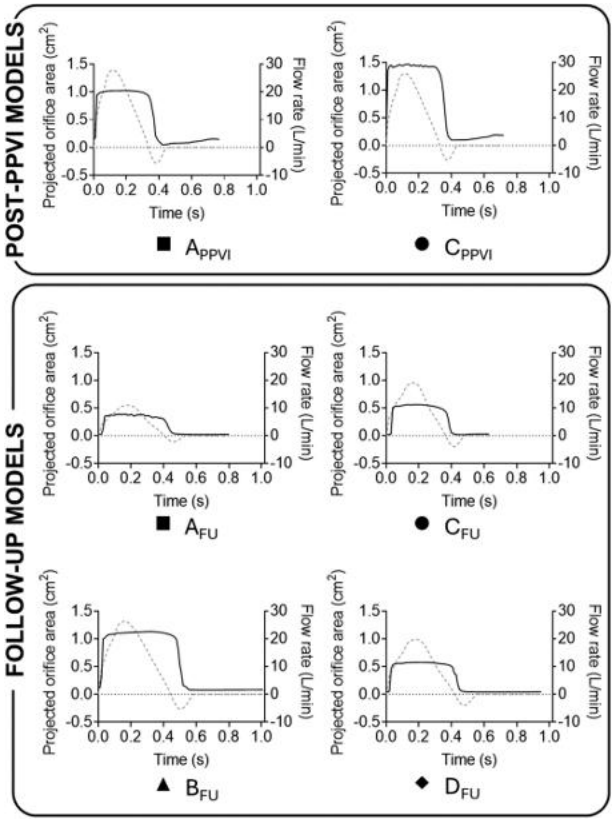


Fig. 11. Projected valve orifice area (solid black line) and flow-rate (dashed gray line) waveforms for the six simulation scenarios.

Despite these limitations, the proposed framework captured key PA hemodynamic patterns and PPV biomechanical features, and highlighted the influence of patient-specific anatomy and baseline hemodynamics on flow organization downstream of implanted PPVs [32], [49]. Future work should extend the cohort size and incorporate prospectively acquired, standardized clinical data. The framework could also be used to explore clinically relevant procedural variables (e.g., PPV orientation and implantation height). Finally, application to additional PPV designs would enable systematic assessment of how device design influences biomechanical response under patient-specific conditions.

V. Conclusion

This study presents a patient-specific FSI framework for simulating PPV behavior using routinely acquired clinical data. The framework was applied to different scenarios, including cases characterized by PPV narrowing. Simulations characterized PA flow organization and leaflets loading, providing complementary biomechanical descriptors beyond clinically available pressure-gradient estimates.

Across cases, patient-specific anatomy and baseline hemodynamics influenced PPV behavior by modulating vorticity transport and helical flow patterns and associated shear environment in PAs. Overall, our findings support the value of patient-specific FSI modelling for PPV biomechanics, particularly in congenital heart disease where anatomy and hemodynamics are highly heterogeneous, and suggest that, with further improvements and validation across a larger patient cohort, the framework could be used to explore device behavior under varying patient-specific and procedural conditions.

References

[1] Y. Liu et al., "Global birth prevalence of congenital heart defects 1970-2017: Updated systematic review and meta-analysis of 260 studies," *Int. J. Epidemiol.*, vol. 48, no. 2, pp. 455–463, Apr. 2019, doi: 10.1093/ije/dyz009.

[2] G. A. Roth et al., "Global burden of cardiovascular diseases and risk factors, 1990-2019: Update From the GBD 2019 Study," *J. Amer. College Cardiol.*, vol. 76, no. 25, pp. 2982–3021, Dec. 2020, doi: 10.1016/j.jacc.2020.11.010.

[3] B. W. Driesen et al., "Percutaneous pulmonary valve implantation: Current status and future perspectives," *Curr. Cardiol. Rev.*, vol. 15, no. 4, pp. 262–273, Jan. 2019, doi: 10.2174/1573403x15666181224113855.

[4] N. D. Patel, D. S. Levi, J. P. Cheatham, S. A. Qureshi, S. Shahanavaz, and E. M. Zahn, "Transcatheter pulmonary valve replacement: A review of current valve technologies," *J. Soc. Cardiovasc. Angiogr. Interv.*, vol. 1, no. 6, Nov. 2022, Art. no. 100452, doi: 10.1016/j.jscai.2022.100452.

[5] M. Megaly et al., "Outcomes of percutaneous and surgical pulmonary valve implantation," *Cardiovasc. Revasc. Med.*, vol. 32, pp. 27–32, Nov. 2021, doi: 10.1016/j.carrev.2020.12.035.

[6] P. Bonhoeffer et al., "Percutaneous replacement of pulmonary valve in a right-ventricle to pulmonary-artery prosthetic conduit with valve dysfunction," *Lancet*, vol. 356, pp. 1403–1405, Oct. 2000, doi: 10.1016/S0140-6736(00)02844-0.

[7] T. Kogure and S. A. Qureshi, "The future of paediatric heart interventions: Where will we be in 2030?," *Curr. Cardiol. Rep.*, vol. 22, Oct. 2020, Art. no. 158, doi: 10.1007/s11886-020-01404-z/Published.

[8] G. J. Krings et al., "Percutaneous pulmonary valve implantation guided by three-dimensional rotational angiography," *Int. J. Cardiol. Congenital Heart Dis.*, vol. 18, Dec. 2024, Art. no. 100541, doi: 10.1016/j.ijcchd.2024.100541.

[9] E. M. Horlick and N. A. Haas, "Percutaneous pulmonary valve replacement: What a difference a day makes," *J. Amer. College Cardiol.*, vol. 76, no. 24, pp. 2859–2861, Dec. 2020, doi: 10.1016/j.jacc.2020.11.003.

[10] N. Agwu, M. R. Recto, and A. Kheradvar, "Unmet clinical needs for transcatheter pulmonary valves," *Ann. Biomed. Eng.*, vol. 51, pp. 2384–2392, Nov. 2023, doi: 10.1007/s10439-023-03328-5.

[11] D. B. McElhinney, A. C. Marshall, and S. Schievano, "Fracture of cardiovascular stents in patients with congenital heart disease," *Circular Cardiovasc. Interv.*, vol. 6, no. 5, pp. 575–585, Oct. 2013, doi: 10.1161/CIRCINTERVENTIONS.113.000148.

[12] J. Nordmeyer et al., "Risk stratification, systematic classification, and anticipatory management strategies for stent fracture after percutaneous pulmonary valve implantation," *Circulation*, vol. 115, no. 11, pp. 1392–1397, Mar. 2007, doi: 10.1161/CIRCULATIONAHA.106.674259.

[13] G. Brancaccio et al., "Investigating the long-term durability of prosthetic valves in patients who have undergone Tetralogy of Fallot surgery with transannular patch," *Interdiscipl. Cardiovasc. Thoracic Surg.*, vol. 40, no. 8, Aug. 2025, Art. no. ivaf159, doi: 10.1093/icvts/ivaf159.

[14] P. Spagnolo et al., "Hypoattenuating leaflet thickening after transcatheter pulmonary valve implantation: An urgent call to action," *JACC Case Rep.*, vol. 30, no. 17, Jul. 2025, Art. no. 103889, doi: 10.1016/j.jaccas.2025.103889.

[15] G. M. Bosi, C. Capelli, S. Khambadkone, A. M. Taylor, and S. Schievano, "Patient-specific finite element models to support clinical decisions: A lesson learnt from a case study of percutaneous pulmonary valve implantation," *Catheterization Cardiovasc. Interv.*, vol. 86, no. 6, pp. 1120–1130, Nov. 2015, doi: 10.1002/ccd.25944.

[16] C. Capelli, A. M. Taylor, F. Migliavacca, P. Bonhoeffer, and S. Schievano, "Patient-specific reconstructed anatomies and computer simulations are fundamental for selecting medical device treatment: Application to a new percutaneous pulmonary valve," *Philos. Trans. Ser. A. Math. Phys. Eng. Sci.*, vol. 368, pp. 3027–3038, Jun. 2010, doi: 10.1098/rsta.2010.0088.

[17] D. Cosentino et al., "Geometrical and stress analysis of factors associated with stent fracture after melody percutaneous pulmonary valve implantation," *Circular Cardiovasc. Interv.*, vol. 7, pp. 510–517, Aug. 2014, doi: 10.1161/CIRCINTERVENTIONS.113.000631.

[18] S. Schievano et al., "Finite element analysis of stent deployment: Understanding stent fracture in percutaneous pulmonary valve implantation," *J. Interventional Cardiol.*, vol. 20, no. 6, pp. 546–554, Oct. 2007, doi: 10.1111/j.1540-8183.2007.00294.x.

[19] A. Caimi et al., "Prediction of stenting related adverse events through patient-specific finite element modelling," *J. Biomech.*, vol. 79, pp. 135–146, Oct. 2018, doi: 10.1016/j.jbiomech.2018.08.006.

[20] S. M. Baek, K. Choi, S. Y. Lee, H. G. Lim, G. B. Kim, and J. Seo, "Quantitative comparisons of pulmonary artery hemodynamics before and after Pulsta valve implantation in patients with Tetralogy of Fallot using computational fluid dynamics," *Front. Cardiovasc. Med.*, vol. 12, Jun. 2025, Art. no. 1586134, doi: 10.3389/fcvm.2025.1586134.

[21] M. Hirschhorn, V. Tchantchaleishvili, R. Stevens, J. Rossano, and A. Throckmorton, "Fluid–structure interaction modeling in cardiovascular medicine – A systematic review 2017–2019," *Med. Eng. Phys.*, vol. 78, pp. 1–13, Apr. 2020, doi: 10.1016/j.medengphy.2020.01.008.

[22] M. Arminio, D. Carbonaro, U. Morbiducci, D. Gallo, and C. Chiastra, "Fluid-structure interaction simulation of mechanical aortic valves: A narrative review exploring its role in total product life cycle," *Front. Med. Technol.*, vol. 6, Jul. 2024, Art. no. 1399729, doi: 10.3389/fmedt.2024.1399729.

[23] M. S. Zakaria et al., "Review of numerical methods for simulation of mechanical heart valves and the potential for blood clotting," *Med. Biol. Eng. Comput.*, vol. 55, pp. 1519–1548, Sep. 2017, doi: 10.1007/s11517-017-1688-9.

[24] J. S. Soares, K. R. Feaver, W. Zhang, D. Kamensky, A. Aggarwal, and M. S. Sacks, "Biomechanical behavior of bioprosthetic heart valve heterograft tissues: Characterization, simulation, and performance," *Cardiovasc. Eng. Technol.*, vol. 7, pp. 309–351, Dec. 2016, doi: 10.1007/s13239-016-0276-8.

[25] G. Luraghi et al., "On the modeling of patient-specific transcatheter aortic valve replacement: A fluid–structure interaction approach," *Cardiovasc. Eng. Technol.*, vol. 10, no. 3, pp. 437–455, Sep. 2019, doi: 10.1007/s13239-019-00427-0.

[26] G. Luraghi, J. F. Rodriguez Matas, and F. Migliavacca, "In silico approaches for transcatheter aortic valve replacement inspection," *Expert Rev. Cardiovasc. Ther.*, vol. 19, no. 1, pp. 61–70, Jan. 2021, doi: 10.1080/14779072.2021.1850265.

[27] A. Agarwal, L. Ranard, T. Vahl, and O. Khalique, "Advanced computer simulation based on cardiac imaging in planning of structural heart disease interventions," *J. Clin. Med.*, vol. 14, no. 19, Sep. 2025, Art. no. 6885, doi: 10.3390/jcm14196885.

[28] B. Grossi et al., "Predicting procedural outcomes in transcatheter aortic valve implantation: A scoping review of numerical patient-specific simulations," *Prog. Biomed. Eng.*, vol. 8, no. 1, Mar. 2026, Art. no. 012001, doi: 10.1088/2516-1091/ae1772.

[29] P. Wong et al., "Looking towards the future: Patient-specific computational modeling to optimize outcomes for transcatheter mitral valve repair," *Front. Cardiovasc. Med.*, vol. 10, Apr. 2023, Art. no. 1140379, doi: 10.3389/fcvm.2023.1140379.

[30] K. Baylous et al., "Thrombogenic risk assessment of transcatheter prosthetic heart valves using a fluid-structure interaction approach," *Comput. Methods. Programs Biomed.*, vol. 257, Dec. 2024, Art. no. 108469, doi: 10.1016/j.cmpb.2024.108469.

[31] F. Esmailie et al., "Biomechanics of transcatheter aortic valve replacement complications and computational predictive modeling," *Struct. Heart*, vol. 6, no. 2, Jun. 2022, Art. no. 100032, doi: 10.1016/j.shj.2022.100032.

[32] N. K. Schiavone, C. J. Elkins, D. B. McElhinney, J. K. Eaton, and A. L. Marsden, "In vitro assessment of right ventricular outflow tract anatomy and valve orientation effects on bioprosthetic pulmonary valve hemodynamics," *Cardiovasc. Eng. Technol.*, vol. 12, no. 2, pp. 215–231, Apr. 2021, doi: 10.1007/s13239-020-00507-6.

[33] H. L. Oliveira et al., "Three-dimensional fluid–structure interaction simulation of the Wheatley aortic valve," *Int. J. Numer. Method Biomed. Eng.*, vol. 40, no. 2, Feb. 2024, Art. no. e3792, doi: 10.1002/cnm.3792.

[34] M. Arminio et al., "A fluid–structure interaction framework for mechanical aortic valves: Analyzing the effects of valve design and aortic curvature on hemodynamics," *Med. Eng. Phys.*, vol. 147, no. 1, Jan. 2026, Art. no. 015008, doi: 10.1088/1873-4030/ae1e76.

[35] Z. Jalal, L. Galmiche, C. Beloin, and Y. Boudjemline, "Impact of percutaneous pulmonary valve implantation procedural steps on leaflets histology and mechanical behaviour: An in vitro study," *Arch. Cardiovasc. Dis.*, vol. 109, no. 8/9, pp. 465–475, Aug. 2016, doi: 10.1016/j.acvd.2016.01.015.

[36] *Cardiovascular Implants - Cardiac Valve Prostheses - Part 1: General Requirements*, ISO 5840:2021, International Organization for Standardization, Geneva, Switzerland, 2021.

[37] K. B. Ko, J. H. Seo, A. Doshi, D. G. Sen, and R. Mittal, "Computational study on the effects of valve orientation on the hemodynamics and leaflet dynamics of bioprosthetic pulmonary valves," *J. Biomech. Eng.*, vol. 146, no. 12, Dec. 2024, Art. no. 121002, doi: 10.1115/1.4066178.

[38] F. Zhou et al., "Analysis of flow field in mechanical aortic bileaflet heart valves using finite volume method," *J. Med. Biol. Eng.*, vol. 36, pp. 110–120, Feb. 2016, doi: 10.1007/s40846-016-0106-3.

[39] N. Pil, A. G. Kuchumov, B. Kadyraliev, and V. Arutunyan, "Influence of aortic valve leaflet material model on hemodynamic features in healthy and pathological states," *Mathematics*, vol. 11, no. 2, Jan. 2023, Art. no. 428, doi: 10.3390/math11020428.

[40] W. Zhang, J. Liu, Q. Yan, J. Liu, H. Hong, and L. Mao, "Computational haemodynamic analysis of left pulmonary artery angulation effects on pulmonary blood flow," *Interact. Cardiovasc. Thoracic Surg.*, vol. 23, no. 4, pp. 519–525, Oct. 2016, doi: 10.1093/icvts/ivw179.

[41] L. Bontempi et al., "Idealized aortic annuloplasty FSI digital twin of 3D-printed phantoms with 4D-flow MRI comparison," *Comput. Biol. Med.*, vol. 192, Jun. 2025, Art. no. 110398, doi: 10.1016/j.compbiomed.2025.110398.

[42] J. M. Zhan, Y. T. Li, W. H. O. Wai, and W. Q. Hu, "Comparison between the Q criterion and Rortex in the application of an in-stream structure," *Phys. Fluids*, vol. 31, no. 12, Dec. 2019, Art. no. 121701, doi: 10.1063/1.5124245.

[43] P. Corso and D. Obrist, "On the role of aortic valve architecture for physiological hemodynamics and valve replacement, Part I: Flow configuration and vortex dynamics," *Comput. Biol. Med.*, vol. 176, Jun. 2024, Art. no. 108526, doi: 10.1016/j.compbiomed.2024.108526.

[44] P. Petitjeans, "Stretching of a vortical structure: Filaments of vorticity," *Europhys. News*, vol. 34, no. 1, pp. 20–23, 2003.

[45] D. Gallo, D. A. Steinman, P. B. Bijari, and U. Morbiducci, "Helical flow in carotid bifurcation as surrogate marker of exposure to disturbed shear," *J. Biomech.*, vol. 45, no. 14, pp. 2398–2404, Sep. 2012, doi: 10.1016/j.jbiomech.2012.07.007.

[46] Z. A. Wei, M. Tree, P. M. Trusty, W. Wu, S. Singh-Gryzbon, and A. Yoganathan, "The advantages of viscous dissipation rate over simplified power loss as a Fontan hemodynamic metric," *Ann. Biomed. Eng.*, vol. 46, no. 3, pp. 404–416, Mar. 2018, doi: 10.1007/s10439-017-1950-1.

[47] D. Hasler and D. Obrist, "Three-dimensional flow structures past a bioprosthetic valve in an in-vitro model of the aortic root," *Plos One*, vol. 13, no. 3, Mar. 2018, Art. no. e0194384, doi: 10.1371/journal.pone.0194384.

[48] E. L. Johnson et al., "Parameterization, geometric modeling, and isogeometric analysis of tricuspid valves," *Comput. Methods Appl. Mech. Eng.*, vol. 384, Oct. 2021, Art. no. 113960, doi: 10.1016/j.cma.2021.113960.

[49] E. Criseo, I. Fumagalli, A. Quarteroni, S. M. Marianeschi, and C. Vergara, "Computational haemodynamics for pulmonary valve replacement by means of a reduced fluid-structure interaction model," *Int. J. Numer. Method. Biomed. Eng.*, vol. 40, no. 9, Sep. 2024, Art. no. e1846, doi: 10.1002/cnm.3846.

[50] A. D. Kaiser, N. K. Schiavone, C. J. Elkins, D. B. McElhinney, J. K. Eaton, and A. L. Marsden, "Comparison of immersed boundary simulations of heart valve hemodynamics against in vitro 4D flow MRI data," *Ann. Biomed. Eng.*, vol. 51, no. 10, pp. 2267–2288, Oct. 2023, doi: 10.1007/s10439-023-03266-2.

[51] I. Borazjani, "A review of fluid-structure interaction simulations of prosthetic heart valves," *J. Long Term Effects Med. Implants*, vol. 25, no. 2, pp. 75–93, 2015, doi: 10.1615/jlongtermeffmedimplants.2015011791.

[52] P. De Jaegere, G. Rocatello, B. D. Prendergast, O. De Backer, N. M. Van Mieghem, and R. Rajani, "Patient-specific computer simulation for transcatheter cardiac interventions: What a clinician needs to know," *Heart*, vol. 105, pp. s21–s27, Mar. 2019, doi: 10.1136/heartjnl-2018-313514.

[53] National Institute for Health and Clinical Excellence, "Interventional procedure overview of percutaneous pulmonary valve implantation for right ventricular outflow tract dysfunction," 2012. Accessed: Jul. 8, 2026. [Online]. Available: https://www.nice.org.uk/guidance/htg297/evidence

[54] H. Baumgartner et al., "2020 ESC Guidelines for the management of adult congenital heart disease," *Eur. Heart J.*, vol. 42, pp. 563–645, Feb. 2021, doi: 10.1093/eurheartj/ehaa554.

[55] F. Sotiropoulos, T. B. Le, and A. Gilmanov, "Fluid mechanics of heart valves and their replacements," *Annu. Rev. Fluid Mech.*, vol. 48, pp. 259–283, Jan. 2016, doi: 10.1146/annurev-fluid-122414-034314.

[56] H. Chen, M. Samaee, M. Tree, L. Dasi, and A. Yoganathan, "Hemodynamics of the VenusP valve system™ – An in vitro study," *Front. Med. Technol.*, vol. 6, May 2024, Art. no. 1376649, doi: 10.3389/fmedt.2024.1376649.

[57] G. Reiter et al., "Magnetic resonance-derived 3-dimensional blood flow patterns in the main pulmonary artery as a marker of pulmonary hypertension and a measure of elevated mean pulmonary arterial pressure," *Circular Cardiovasc. Imag.*, vol. 1, no. 1, pp. 23–30, Jul. 2008, doi: 10.1161/CIRCIMAGING.108.780247.

[58] F. Capuano, Y. H. Loke, and E. Balaras, "Blood flow dynamics at the pulmonary artery bifurcation," *Fluids*, vol. 4, no. 4, Nov. 2019, Art. no. 190, doi: 10.3390/fluids4040190.

[59] S. Mosbahi et al., "Computational fluid dynamics of the right ventricular outflow tract and of the pulmonary artery: A bench model of flow dynamics," *Interactive Cardiovasc. Thoracic Surg.*, vol. 19, no. 4, pp. 611–616, Oct. 2014, doi: 10.1093/icvts/ivu202.

[60] H. Gbinigie, L. Coats, J. D. Parikh, K. G. Hollingsworth, and L. Gan, "A 4D flow cardiovascular magnetic resonance study of flow asymmetry and haemodynamic quantity correlations in the pulmonary artery," *Physiol. Meas.*, vol. 42, no. 2, Feb. 2021, Art. no. 025005, doi: 10.1088/1361-6579/abdf3b.

[61] J. Geiger et al., "4D-MR flow analysis in patients after repair for tetralogy of Fallot," *Eur. Radiol.*, vol. 21, pp. 1651–1657, Aug. 2011, doi: 10.1007/s00330-011-2108-4.

[62] P. Bächler et al., "Assessment of normal flow patterns in the pulmonary circulation by using 4D magnetic resonance velocity mapping," *Magn. Reson. Imag.*, vol. 31, no. 2, pp. 178–188, Feb. 2013, doi: 10.1016/j.mri.2012.06.036.

[63] M. Sabry et al., "Vortex duration in the pulmonary artery does not depend on vascular afterload: A sign of adaptation?," *Comput. Biol. Med.*, vol. 196, Sep. 2025, Art. no. 110717, doi: 10.1016/j.compbiomed.2025.110717.

[64] V. Peiffer, S. J. Sherwin, and P. D. Weinberg, "Does low and oscillatory wall shear stress correlate spatially with early atherosclerosis? A systematic review," *Cardiovasc. Res.*, vol. 92, pp. 242–250, Jul. 2013, doi: 10.1093/cvr/cvt044.

[65] U. Morbiducci, A. M. Kok, B. R. Kwak, P. H. Stone, D. A. Steinman, and J. J. Wentzel, "Atherosclerosis at arterial bifurcations: Evidence for the role of haemodynamics and geometry," *Thromb. Haemostasis*, vol. 115, pp. 484–492, Mar. 2016, doi: 10.1160/TH15-07-0597.

[66] E. L. Johnson, M. R. Rajanna, C. H. Yang, and M. C. Hsu, "Effects of membrane and flexural stiffnesses on aortic valve dynamics: Identifying the mechanics of leaflet flutter in thinner biological tissues," *Forces Mech.*, vol. 6, Feb. 2022, Art. no. 100053, doi: 10.1016/j.finmec.2021.100053.

[67] S. Schievano et al., "Patient specific finite element analysis results in more accurate prediction of stent fractures: Application to percutaneous pulmonary valve implantation," *J. Biomech.*, vol. 43, no. 4, pp. 687–693, Mar. 2010, doi: 10.1016/j.jbiomech.2009.10.024.

[68] C. Capelli et al., "Patient-specific simulations for planning treatment in congenital heart disease," *Interface Focus*, vol. 8, Feb. 2018, Art. no. 20170021, doi: 10.1098/rsfs.2017.0021.

[69] C. L. Donahue, C. L. Westman, B. L. Faanes, A. M. Qureshi, V. H. Barocas, and V. Aggarwal, "Finite element modeling with patient-specific geometry to assess clinical risks of percutaneous pulmonary valve implantation," *Catheterization Cardiovasc. Interv.*, vol. 103, no. 6, pp. 924–933, May 2024, doi: 10.1002/ccd.31016.

[70] C. E. Pérez-Cualtán, C. Castro-Páez, C. E. Guerrero-Chalela, P. A. Iaizzo, J. Navarro-Rueda, and J. C. Briceño, "The role of 3D printing and finite element-based computational simulations in transcatheter pulmonary valve replacement," *Prog. Biomed. Eng.*, vol. 7, no. 4, Oct. 2025, Art. no. 042007, doi: 10.1088/2516-1091/adfbcb.

[71] M. Toma, S. Singh-Gryzbon, E. Frankini, Z. Wei, and A. P. Yoganathan, "Clinical impact of computational heart valve models," *Materials*, vol. 15, no. 9, May 2022, Art. no. 3302, doi: 10.3390/ma15093302.

[72] H. S. Huang and J. Lu, "Biaxial mechanical properties of bovine jugular venous valve leaflet tissues," *Biomech. Model Mechanobiol.*, vol. 16, no. 6, pp. 1911–1923, Dec. 2017, doi: 10.1007/s10237-017-0927-1.